

---

# MULTI-LAYER WIND VELOCITY FIELD VISUALIZATION IN INFRARED IMAGES OF CLOUDS

---

**Guillermo Terrén-Serrano**

Department of Electrical and Computer Engineering  
The University of New Mexico  
Albuquerque, NM 87131, United States  
guillermoterren@unm.edu

**Manel Martínez-Ramón**

Department of Electrical and Computer Engineering  
The University of New Mexico  
Albuquerque, NM 87131, United States  
manel@unm.edu

March 13, 2022

## ABSTRACT

The energy available in a solar energy powered grid is related to the weather conditions at the time of generation. The forecast of Global Solar Irradiance (GSI) provides the power grid with the capability of scheduling the dispatch of energy. This article investigates how to infer multiple wind velocity fields using consecutive longwave infrared (IR) images of clouds. The objective is to forecast the occlusion of the Sun by clouds. Unsupervised learning is implemented to infer the distribution of the clouds' velocity vectors and heights in multiple wind velocity fields in an IR image. A Multi-Output Weighted Support Vector Machine with Flow Constrains ( $\epsilon$ -MO-WSVM-FC) is used to extrapolate the wind velocity fields to the entire frame, visualizing the path of the clouds. The proposed algorithm is capable of approximating the wind velocity using the velocity vectors and physical features of clouds extracted from IR images. It is possible to forecast Sun occlusions when the wind velocity field is approximated in a small air parcel with the assumption that the streamlines are pathlines.

**Keywords** Cloud Tracking · Machine Learning · Flow Visualization · Beta Mixture Model · Sky Imaging · Solar Forecasting

## 1 Introduction

Recent legislative initiatives to stimulate the use of solar power and other sustainable energy sources in the United States will increase the number of solar power plants connected to the Western Interconnection. California aims to have 100% of clean energy generation by 2045 [1]. Similar initiatives are occurring in Japan and the European Union, where local governments aim to generate the 24%, and 32% of their energy from renewable sources by 2030 respectively [2, 3]. In addition, the growth of Photovoltaic (PV) solar power capacity continues increasing in a steady exponential scale from 2000 [4].

To increase the percentage of solar energy in the electrical power grid it is important to guarantee a reliable supply of energy [5]. The forecasting of solar power provides a Smart Grid (SG) with the capability of performing energy management [6]. The interruptions in energy supply from their PV systems occurs due to the projection of shadows from passing clouds [7]. In particular, the forecasting of solar irradiance in Micro Grids [8, 9] allows automatic control of home appliances and other devices [10]. In fact, moving clouds have different effects depending on the configuration of PV arrays [11], and may cause the solar irradiance received by a PV system to increase or decrease [12]. In a large-scale SG with a stable supply of energy using a mix plan of solar power from PV, concentrated solar power [13] and other systems, the forecasting of solar energy is necessary to perform an efficient management of the resources [14].

There is a documented relationship between ground measurements of Direct Normal Irradiance (DNI) and Cloud Index (CI) [15]. The relationship holds in diverse climates and weather conditions [16, 17, 18] when the CI is calculated from visible (VI) and IR light sensors mounted in geostationary satellites [19, 16, 20, 21, 17, 18, 22]. On-ground maps of solar irradiance can be derived from the CI using geostationary satellite images [23, 24].

This research aims to visualize the wind velocity field to anticipate interruptions in the supply of energy generated by PV systems [25, 26]. The forecasting interval of this application is from 1 to 5 minutes [25]. This is often called nowcasting [27]. Accurate Numerical Weather Prediction models (NWP) which analyze atmospheric dynamics using satellite images are computationally expensive due to the resolution of the numerical grid necessary to analyze the forecasting intervals [28]. The variables in Mesoscale Meteorology models (MM) have collinearity when the objective is to forecast solar irradiation [29].

When transmitting images from a satellite, communications might have a delay of up to an hour [17]. An alternative to satellite images is Total Sky Imagery (TSI) [30, 31]. This device captures sky images reflected on a concave mirror, and allows a high Field Of View (FOV). This device has a number of disadvantages including its cost, and the projection of shadows on the mirror from objects in its own structure [32, 33]. Digital cameras are less expensive, and by attaching lenses to them, can obtain better performances around the circumsolar area [34]. In fact, near IR filters can attenuate the scattering produced by solar irradiance [25], and fish-eye lenses increase the FOV, which allows recording of low-cost, shadow-free sky images [35, 36]. IR sensors are a the most liable alternative when the forecast is meant for hours ahead, and includes night hours or pour daylight conditions [37]. Recent technological innovations increased ground-based IR images FOV [38].

The visualization of the wind velocity field requires to measure the wind velocity at a given altitude. The wind velocity gradient increases with the altitude in the lower atmosphere [39]. The decrease of temperature along the Troposphere can be approximated by a linear function [40]. Cloud formations are feasible in a range of altitudes that varies from the ground to the Tropopause [41]. The detection of clouds in IR images allows us to indirectly measure physical magnitudes of the wind velocity field [42]. Radiometric IR cameras provide uniform thermal imaginary [43], and may be stabilized to perform atmospheric measurements [44]. In fact, microbolometer IR cameras have been used in the statistical analysis of clouds [45] in application of Earth-space communications [46].

Methods of computational numerical analysis are an effective way to analyze clouds images. The direction and magnitude of cloud velocity have been estimated applying motion vector techniques to a series of consecutive frames [19, 32, 16, 17, 33, 18]. Through image segmentation it is possible to identify clouds and other objects in an image [36, 34, 33]. The clouds' pathlines can be estimated tracking with a Kalman filter [36]. Classical methods of statistical modeling and linear regression have low computational requirements, and they are an alternative to complex NWP models [32, 37, 47, 20, 33, 18, 22]. Machine Learning (ML) algorithms such as Artificial Neural Networks (ANN) [25, 26, 48], or Support Vector Machines (SVM) [17, 49], are promising models to find space-time correlations in cloud images.

The method proposed in this research utilizes an innovative system for capturing circumsolar images that combines pyranometer measurements and IR images [50]. It is equipped with a solar tracker that updates its pan and tilt every second, maintaining the sun in a central position in the images during the day [51]. The IR images are taken at an angle from the normal position of the camera in relation to the ground. This angle is the sun's zenith angle. This causes the relative distance of a given object on horizon to increase from top to bottom in an image. In order to account for this effect, it is implemented a geometrical transformation of the velocity vectors from the original Euclidean frame of reference, to a non-linear frame of reference.

This investigation proposes a method to infer the distribution of the velocity vectors and heights when there are multiple layers of clouds in an image. Segmentation and subsampling of velocity vectors are implemented to reduce both the noise in velocity vectors and the computation burden in flow approximation. A formulation of a Multi-Output Weighted Support Vector Machine ( $\epsilon$ -MO-WSVM) [52, 53, 54, 55] modified from its original form adding flow constrains is introduced to approximate non-turbulent flows. The method implemented in this investigation is based on fluid dynamics.

## 2 Wind Velocity Field

The IR sensor provides an uniform thermal image as output. When the radiometry functionality is enabled the pixels in a frame, are turned into temperature measurements. A pixel of the camera frame is defined by a pair of euclidean coordinates  $\mathbf{X} = \{(x, y)_{i,j} \mid \forall i = 1, \dots, M, \forall j = 1, \dots, N\}$ , and the temperature of each one of the pixels is defined in Kelvin degrees as  $\mathbf{T}^k = \{T_{i,j} \in \mathbb{R} \mid \forall i = 1, \dots, M, \forall j = 1, \dots, N\}$ , where  $k$  represents a process defined as  $k \in (0, \infty]$ , that is a sequence of IR images ordered chronologically by capturing time. The temperature of a particle in the Troposphere is a function of the height [56]. The height of a pixel in a frame can be approximated using the Moist Adiabatic Lapse Rate (MALR) function [50], that we define as  $\phi : T \mapsto h$ , knowing the temperatures obtained with the IR camera. The height of each one of the pixels in a frame are  $\mathbf{H}^k = \{H_{i,j} \in \mathbb{R} \mid \forall i = 1, \dots, M, \forall j = 1, \dots, N\}$ .

When there are multiple layers of clouds in an image, a Beta Mixture Model (BeMM) of the temperature of the pixels is expected to have multiple clusters. The number of clusters  $C$  is estimated by a previously trained detection algorithm that does inference over the number of wind velocity fields which are in an image. In order to infer the distribution of the temperature of the pixels with a BeMM, these are first normalized to the domain of a beta distribution such as  $\bar{T}_{i,j} = [T_{i,j} - \min(\mathbf{T}^k)] / [\max(\mathbf{T}^k) - \min(\mathbf{T}^k)]$ .

## 2.1 Beta Mixture Model

Consider the temperatures  $\bar{T}_{i,j}$  of a given image (by omitting superindex  $k$ ). The distribution of the normalized heights can be approximated by mixture of beta distributions  $\bar{T} \sim Be(\alpha_c, \beta_c)$  which density function is,

$$f(\bar{T}_{i,j}; \alpha_c, \beta_c) = \frac{1}{B(\alpha_c, \beta_c)} \cdot \bar{T}_{i,j}^{\alpha_c-1} \cdot (1 - \bar{T}_{i,j})^{\beta_c-1}, \quad \alpha_c, \beta_c > 0, \quad (1)$$

where  $\bar{T}_{i,j} \in (0, 1)$ , beta function is  $B(\alpha_c, \beta_c) = [\Gamma(\alpha_c)\Gamma(\beta_c)] / [\Gamma(\alpha_c + \beta_c)]$ , and the gamma function is  $\Gamma(\alpha_c) = (\alpha_c - 1)!$ .

The log-likelihood of the beta density function, that we need to compute the expected complete data log-likelihood (CDLL),

$$\log p(\bar{T}_{i,j} | \alpha_c, \beta_c) = (\alpha_c - 1) \log \bar{T}_{i,j} + (\beta_c - 1) \log (1 - \bar{T}_{i,j}) - \log B(\alpha_c, \beta_c), \quad (2)$$

and CDLL in the mixture model is,

$$\mathcal{Q}(\boldsymbol{\theta}^{(t)}, \boldsymbol{\theta}^{(t-1)}) = \sum_{i=1}^M \sum_{j=1}^N \sum_{c=1}^C \gamma_{i,j,c} \log \pi_c + \sum_{i=1}^M \sum_{j=1}^N \sum_{c=1}^C \gamma_{i,j,c} \log p(\bar{T}_{i,j} | \boldsymbol{\theta}^{(t)}) \quad (3)$$

where  $\gamma_{i,j,c} \triangleq p(y_{i,j} = c | \bar{T}_{i,j}, \boldsymbol{\theta}^{(t-1)})$  is the responsibility of the cluster  $c$  in the sample  $i, j$  and  $\boldsymbol{\theta}^{(t)} = \{\alpha_c^{(t)}, \beta_c^{(t)}\}$ .

The parameters in the clustering of beta distributions can be directly computed applying the Expectation Maximization (EM) algorithm [57, 58]. In the E stage of the algorithm a prior is established and then, by using the likelihood function (3), a posterior  $\gamma_{i,j,c} = p(y_{i,j} = c | \bar{T}_{i,j}, \boldsymbol{\theta})$  can be assigned to each sample. In the M stage, the parameters  $\alpha_c$  and  $\beta_c$  of each cluster that maximize the log-likelihood are computed by gradient descent of the CDLL [59]. The corresponding derivatives are,

$$\frac{\partial \mathcal{L}(\boldsymbol{\theta})}{\partial \alpha_c} = \sum_{i=1}^M \sum_{j=1}^N \sum_{c=1}^C \gamma_{i,j,c} \frac{\partial}{\partial \alpha_c} \log p(\bar{T}_{i,j} | \alpha_c, \beta_c) \quad (4)$$

$$= \sum_{i=1}^M \sum_{j=1}^N \gamma_{i,j,c} \sum_{c=1}^C [\log \bar{T}_{i,j} - \psi(\alpha_c) + \psi(\alpha_c + \beta_c)], \quad (5)$$

$$\frac{\partial \mathcal{L}(\boldsymbol{\theta}_c)}{\partial \beta_c} = \sum_{i=1}^M \sum_{j=1}^N \sum_{c=1}^C \gamma_{i,j,c} \left[ \frac{\partial}{\partial \beta_c} \log p(\bar{T}_{i,j} | \alpha_c, \beta_c) \right] \quad (6)$$

$$= \sum_{i=1}^M \sum_{j=1}^N \gamma_{i,j,c} \sum_{c=1}^C [\log (1 - \bar{T}_{i,j}) - \psi(\beta_c) + \psi(\alpha_c + \beta_c)]. \quad (7)$$

where  $\partial B(\alpha_c, \beta_c) / \partial \alpha_c = B(\alpha_c, \beta_c) \cdot [\psi(\alpha_c) - \psi(\alpha_c + \beta_c)]$ , and  $\psi(\cdot)$  is the digamma function, which is  $\psi(\alpha_c) = \Gamma'(\alpha_c) / \Gamma(\alpha_c)$ .

The optimal priors are found by maximizing the CDLL with respect to  $\pi_c$ , constrained to  $\sum_c \pi_c = 1$ . As a result, the optimal priors are

$$\pi_c = \frac{1}{MN} \sum_{i=1}^M \sum_{j=1}^N \gamma_{i,j,c}. \quad (8)$$

The cloud average heights in a frame are computed using the posterior probabilities  $\gamma_{i,j,c}$  a frame, but only in the pixels that has a cloud,

$$\hat{H}_c = \frac{\sum_{i,j} \gamma_{i,j,c} \cdot H_{i,j} \cdot \mathbb{I}(b_{i,j} = 1)}{\sum_{i,j} \gamma_{i,j,c} \cdot \mathbb{I}(b_{i,j} = 1)}. \quad (9)$$

where  $\mathbb{I}(\cdot)$  is the indicator function. An image segmentation algorithm indicates which pixels belong a cloud, so that  $\mathbf{B} = \{b_{i,j} \in \mathbb{B} \mid \forall i = 1, \dots, M, \forall j = 1, \dots, N\}$  is a binary image where 0 is a clear sky pixel, and 1 is a pixels belonging to a cloud.

The performance of a Gamma Mixture Model and a BeMM were compared to infer the distribution of the temperatures and the heights. In the task of identify which pixels belong to the wind velocity layer, the BeMM of the temperature of the pixels was found to be better.

## 2.2 Motion Vectors

In current computer vision literature, there are three primary methods to estimate the motion of objects in a sequence of images: Lucas-Kanade [60], Horn-Schunk [61], and Farnerback [62]. These three methods are based on the space-time partial derivatives between two consecutive frames. Taking a different disciplinary approach, the velocity field in experimental fluid dynamics is approximated applying research methods based on signal cross-correlation operated in the frequency domain [63]. The techniques to estimate the motion vectors in an image are sensitive to the intensity gradient of the pixels. We implemented a model that removes the gradient produced by the solar direct radiation, and atmospheric scattered radiation. Both of which routinely appear on the images in the course of the year. A persistent model of the window of the camera removes sporadic artifacts that appear in the image such as water spots, or dust particles [50].

A series of sequences of images with clouds flowing in different directions were simulated to cross-validate the set of parameters for each one of the mentioned methods. The investigation searched for a dense implementation of a motion vector method to approximate the dynamics of a cloud. The most suitable method was found to be the Weighted Lucas-Kanade (WLK) [64], but instead of weighting the neighboring pixels with a multivariate normal distribution, the weights  $\gamma_{i,j,c}$  are the posterior probabilities of the BeMM in this application. Therefore, a pixel has a velocity vector for each cloud layer  $c$  in a frame. The optimal window size, weighted least-squares regularization, and differential kernel amplitude are:  $\mathcal{W} = 16$  [pixels<sup>2</sup>],  $\tau = 1 \times 10^{-8}$ , and  $\sigma = 1$  respectively. The velocity components in the x-axis are  $\mathbf{U}_c = \{u_{i,j,c} \in \mathbb{R} \mid \forall i = 1, \dots, M, \forall j = 1, \dots, N\}$ , and the velocity components in y-axis are  $\mathbf{V}_c = \{v_{i,j,c} \in \mathbb{R} \mid \forall i = 1, \dots, M, \forall j = 1, \dots, N\}$ . The units of velocity vectors are in pixels per frame, but knowing the geometrical transformation of the frame, they can be transformed to meters per second [50]. The geometric transformation is a function of the Sun's elevation and azimuth angles  $\psi : (\varepsilon, \alpha) \mapsto \Delta \mathbf{x}_{i,j}$  in a frame, it defines the dimensions of a pixel at a given height  $\Delta \mathbf{X} = \{(\Delta x, \Delta y)_{i,j} \mid \forall i = 1, \dots, M, \forall j = 1, \dots, N\}$ . This transformation connects the coordinates system in x,y-axis with the height, which is z-axis. The relation holds even when the height is an approximation, since the components of velocity vectors are transformed w.r.t. that coordinates system. The velocity vectors of each cloud layer are transformed such as,

$$u_{i,j} = \frac{\delta}{f_r} \cdot \Delta x_{i,j} \sum_{c=1}^C \hat{H}_c \cdot \gamma_{i,j,c} \cdot u_{i,j,c} \quad (10)$$

$$v_{i,j} = \frac{\delta}{f_r} \cdot \Delta y_{i,j} \sum_{c=1}^C \hat{H}_c \cdot \gamma_{i,j,c} \cdot v_{i,j,c} \quad (11)$$

where  $f_r$  is the frame rate of the sequence of images, and  $\delta$  is velocity vectors' scale in the WLK approximation.

## 2.3 Velocity Vectors Selection

In order to approximate the potential, and streamlines of the wind velocity field in a frame, we propose to select the most consistent velocity vectors over a sequence of consecutive frames. The main problems with this approach are that, as the vectors are selected over a sequence of images, the amount of vectors is expected to be large, plus when optical flow is implemented in dense manner, it yields to noisy vectors. Because of that, we threshold the velocity vectors to reduce both the algorithm's computation burden and the variance of the noise.

### 2.3.1 Velocity Vector Segmentation

The pixel intensity difference between two consecutive frames is computed to find the pixels that show a change. The pixel normalized intensities that were used to compute the velocity vectors are  $\mathbf{I} = \{i_{i,j} \in \mathbb{R}^{[0,2^8]} \mid \forall i =$

$1, \dots, M, \forall j = 1, \dots, N\}$ . Its root squared intensity normalized difference is,

$$d_{i,j} = \frac{\sqrt{(i_{i,j}^{k-1} - i_{i,j}^k)^2}}{\sum_{i,j} \sqrt{(i_{i,j}^{k-1} - i_{i,j}^k)^2}} \quad (12)$$

Matrix  $\mathbf{D}$  with normalized differentials  $d_{i,j}$  is vectorized and sorted from the lowest to the highest, i.e.,  $\mathbf{d} = \text{sort}(\text{vec}(\mathbf{D}))$ . A vector  $\mathbf{r}$  with the accumulated variance is computed as

$$r_m = \left\{ \sum_{i=1}^m \mathbf{d}_i \right\}_{m=1}^{N \cdot M}. \quad (13)$$

Then, vector  $\mathbf{r}$  is reorganized and set in the original matrix form, defined as  $\mathbf{R} = \{r_{i,j} \in \mathbb{R}^{[0,1]} \mid \forall i = 1, \dots, M, \forall j = 1, \dots, N\}$ . Finally, a threshold  $\tau$  is applied

$$b_{i,j} = \begin{cases} 1 & r_{i,j} \geq \tau \\ 0 & \text{Otherwise,} \end{cases} \quad (14)$$

where  $\mathbf{B} \in \mathbb{B}$  is a binary image whose elements are 1 when a pixel is select. The thresholded velocity vectors in a frame  $k$  are  $\mathbf{V}'^k = \{\mathbf{v}_{i,j}^k = \{u_{i,j}^k, v_{i,j}^k\} \wedge b_{i,j}^k = 1 \mid \forall i = 1, \dots, M, \forall j = 1, \dots, N\}$ .

Based on the assumption that a cloud floating in the air follows a trajectory dictated by the wind velocity field, the wind velocity field is approximated using the segmented velocity vectors of  $\ell$  last frames. Hence, the set of velocity vectors available to compute the wind velocity field are,

$$\tilde{\mathbf{V}}^k = \begin{bmatrix} \mathbf{V}'^k \\ \vdots \\ \mathbf{V}'^{k-\ell} \end{bmatrix} \in \mathbb{R}^{2 \times N^k}, \quad (15)$$

the number of samples in  $\tilde{\mathbf{V}}^k$  is  $N^k$ , this number is not the same in each frame  $k$ .

### 2.3.2 Velocity Vector and Height Distributions

A velocity vector  $\tilde{\mathbf{v}}_i$  (by omitting superindex  $k$ ) in the set  $\tilde{\mathbf{V}}^k = \{\tilde{\mathbf{v}}_i^k \in \mathbb{R}^2 \mid \forall i = 1, \dots, N^k\}$  is assumed to belong to a cloud layer  $c$ . The probability of a vector to belong to a cloud layer  $c$  is modelled as an independent normal random variable  $\tilde{\mathbf{v}}_i \sim \mathcal{N}(\boldsymbol{\mu}_c, \boldsymbol{\Sigma}_c)$ . The function of the multivariate normal distribution is,

$$p(\tilde{\mathbf{v}}_i \mid \boldsymbol{\mu}_c, \boldsymbol{\Sigma}_c) = \frac{1}{\sqrt{(2\pi)^d |\boldsymbol{\Sigma}_c|}} \cdot \exp \left\{ -\frac{1}{2} (\tilde{\mathbf{v}}_i - \boldsymbol{\mu}_c)^\top \boldsymbol{\Sigma}_c^{-1} (\tilde{\mathbf{v}}_i - \boldsymbol{\mu}_c) \right\}. \quad (16)$$

In the case when two cloud layers were detected, we propose to infer the probability distribution of velocity vectors' in each cloud layer with this model,

$$p(\tilde{\mathbf{v}}_i \mid \boldsymbol{\Theta}) \propto p(\tilde{\mathbf{v}}_i \mid \boldsymbol{\mu}_1, \boldsymbol{\Sigma}_1)^{\lambda_i} \cdot p(\tilde{\mathbf{v}}_i \mid \boldsymbol{\mu}_2, \boldsymbol{\Sigma}_2)^{(1-\lambda_i)}, \quad (17)$$

where  $\boldsymbol{\Theta} = \{\boldsymbol{\lambda}, \boldsymbol{\mu}_1, \boldsymbol{\Sigma}_1, \boldsymbol{\mu}_2, \boldsymbol{\Sigma}_2\}$ , and  $\lambda_i \in \{0, 1\}$ .  $\lambda_{i,c}$  is defined as convex, considering that a velocity vector may belong to one or the other wind velocity layer, but no to both. Knowing the vectors that belong to the first cloud layer, the vectors that belong to the second cloud layer are also known,  $\lambda_{i,2} = 1 - \lambda_{i,1}$ . The lower bound of the data log-likelihood is found applying Jensen's inequality [65],

$$\log p(\tilde{\mathbf{v}}_i \mid \boldsymbol{\Theta}) \propto \lambda_{i,1} \cdot \log p(\tilde{\mathbf{v}}_i \mid \boldsymbol{\mu}_1, \boldsymbol{\Sigma}_1) + \lambda_{i,2} \cdot \log p(\tilde{\mathbf{v}}_i \mid \boldsymbol{\mu}_2, \boldsymbol{\Sigma}_2), \quad (18)$$

so that the posterior distribution is a linear combination of the multivariate normal distributions.

The probabilistic model parameters are inferred using a fixed-point variation of the Independent Conditional Modes (ICM) [66]. The algorithm begins by randomly assigning the velocity vectors to a cloud layer,  $\lambda_{i,1} \sim \mathcal{U}(0, C - 1)$ . The parameters of velocity vector distributions, in Eq. (18) that maximize the data log-likelihood are computed in the first step of the algorithm. These same parameters are used to initialize the inference of the parameters of the height distributions in the second step in Eq. (22).

In the case of a multivariate normal distribution, the ICM algorithm is iteratively updates parameters. At iteration  $t + 1$ , the means and covariances are,

$$\boldsymbol{\mu}_c^{(t+1)} = \frac{\sum_i \lambda_{i,c}^{(t)} \cdot \tilde{\mathbf{v}}_i}{\sum_i \lambda_{i,c}^{(t)}}; \quad \boldsymbol{\Sigma}_c^{(t+1)} = \frac{\sum_i \lambda_{i,c}^{(t)} \cdot \left( \tilde{\mathbf{v}}_i - \boldsymbol{\mu}_c^{(t+1)} \right)^\top \left( \mathbf{v}_i - \tilde{\boldsymbol{\mu}}_c^{(t+1)} \right)}{\sum_i \lambda_{i,c}^{(t)}} \quad (19)$$

The vectors are re-assigned to a cloud layer at the end of each parameters update, applying the maximum a posteriori (MAP) criterion

$$\lambda_{i,2}^{(t+1)} = \underset{c}{\operatorname{argmax}} p \left( \tilde{\mathbf{v}}_i \mid \boldsymbol{\mu}_c^{(t+1)}, \boldsymbol{\Sigma}_c^{(t+1)} \right) - 1 \quad (20)$$

$$\lambda_{i,1}^{(t+1)} = 1 - \lambda_{i,2}^{(t+1)}. \quad (21)$$

After completing the inference of the velocity vectors distribution, it is possible to infer the cloud layer's height using the same method. The velocity vectors in an image were calculated using the WLK method. The algorithm approximates the velocity vector using a set of pixels inside a window. The result is that the velocity vectors do not exactly correspond to a clouds' pixels, which are in motion. Instead, the velocity vectors are assigned to nearby pixels. To identify which layer of clouds  $c$ , is the highest and which one is the lowest, the height distribution of the pixels is inferred using the MAP classification of the velocity vectors  $\mathbf{v}'_{i,j}$  in a image.

The height of the pixels within the cloud are modelled as independently distributed normal random variables  $H_{i,j} \sim \mathcal{N}(\mu_c, \sigma_c^2)$ . The probabilistic model to infer the distribution of heights of each cloud layer in a frame is,

$$\log p(H_{i,j} \mid \boldsymbol{\Theta}) \propto \rho_{i,j,1} \cdot \log p(H_{i,j} \mid \mu_1, \sigma_1^2) + \rho_{i,j,2} \cdot \log p(H_{i,j} \mid \mu_2, \sigma_2^2), \quad (22)$$

where  $\boldsymbol{\Theta} = \{\mathbf{P}, \mu_1, \sigma_1, \mu_2, \sigma_2\}$ , and  $\rho_{i,j,c} \in \{0, 1\}$  is a convex variable so that  $\rho_{i,j,2} = 1 - \rho_{i,j,1}$ .

The ICM algorithm is also used to infer the parameters of the height distributions model. The  $\rho_{i,j,c}$  are initialized to the MAP classification of the velocity vectors  $\mathbf{v}'_{i,j}$  using the parameters that were inferred using all the velocity vectors  $\tilde{\mathbf{v}}_i$  in Eq. (15),

$$\rho_{i,j,2} = \underset{c}{\operatorname{argmax}} p \left( \mathbf{v}'_{i,j} \mid \boldsymbol{\mu}_c, \boldsymbol{\Sigma}_c \right) - 1 \quad (23)$$

$$\rho_{i,j,1} = 1 - \rho_{i,j,2}. \quad (24)$$

The parameters of the height distributions are updated using the formulas in Eq. (19). The algorithm eventually converges so that the pixels in the frame are segmented where a cloud appears. The segmentation is performed according to the MAP classification of height distributions,

$$\rho_{i,j,2}^{(t+1)} = \underset{c}{\operatorname{argmax}} p \left( H_{i,j} \mid \mu_c^{(t+1)}, \sigma_c^{2(t+1)} \right) - 1 \quad (25)$$

$$\rho_{i,j,1}^{(t+1)} = 1 - \rho_{i,j,2}^{(t+1)}. \quad (26)$$

In order to find the height of a given cloud layer, the heights are averaged with this formula,

$$\bar{H}_c = \frac{\sum_{i,j} \rho_{i,j,c} \cdot H_{i,j} \cdot \mathbb{I}(b_{i,j} = 1)}{\sum_{i,j} \rho_{i,j,c} \cdot \mathbb{I}(b_{i,j} = 1)}. \quad (27)$$

The wind velocity fields are organized into upper and lower layers by average height  $\bar{H}_c$ . In this way, each detected wind velocity field has a distribution of velocity vectors, and another distribution of heights.

### 2.3.3 Sampling

In order to reduce the computational burden of the algorithm, a subset of the velocity is selected according to their estimated probability distributions. At each layer  $c$ , we define the importance weights  $w_{i,k}^c$  as

$$w_{i,c}^k \triangleq p(\tilde{\mathbf{v}}_i^k \mid \boldsymbol{\theta}_c), \quad w_{i,c}^k \in \mathbb{R}^+. \quad (28)$$

The weights are normalized to have the probabilities of a probability mass function such as  $\sum_{i=1}^{N_k} \hat{w}_{i,c}^k = 1$ .

The cumulative probability function (CDF) is computed as

$$\tilde{w}_{i,c}^k = \left\{ \sum_{m=1}^i \hat{w}_{m,c}^k \right\}_{i=1}^{N^k}. \quad (29)$$

In order to select samples for each distribution  $p(\tilde{\mathbf{v}}_i^k | \boldsymbol{\theta}_c)$ ,  $N^*/C$  samples are drawn from a uniform distribution,

$$z_{j,c}^k \sim \mathcal{U}(0, 1), \quad j = 1, \dots, \frac{N^*}{C}, \quad (30)$$

For each value  $z_{j,c}^k$ , a sample is selected with the criterion

$$I_{j,c}^k = \operatorname{argmin}_i |\tilde{w}_{i,c}^k - z_{j,c}^k|, \quad \forall i = 1, \dots, N_k \quad \forall j = 1, \dots, \frac{N^*}{C}. \quad (31)$$

The selected vectors are the ones whose CDF is the closest to the values of the uniform samples  $z_{j,c}^k$ ,

$$\tilde{\mathbf{v}}_c^{*k} \triangleq \tilde{\mathbf{v}}_{I_{j,c}^k}^k, \quad \forall j = 1, \dots, \frac{N^*}{C}. \quad (32)$$

The subset of selected velocity vectors in frame  $k$  for the cloud layer  $c$  is  $\mathbf{V}_c^{*k} = \{(\tilde{u}, \tilde{v})_{j,c}^{*k} \in \mathbb{R}^2 \mid \forall j = 1, \dots, N^*/C\}$ , the subset of Euclidean coordinate pairs of those selected vectors is  $\mathbf{X}_c^{*k} = \{(x, y)_{j,c}^{*k} \in \mathbb{N}^2 \mid \forall j = 1, \dots, N^*/C\}$ .

Assuming that the prior is uniform the posterior probabilities are,

$$z_{i,c}^{*k} \triangleq \frac{p(\tilde{\mathbf{v}}_i^{*k} | \boldsymbol{\theta}_c)}{\sum_{c=1}^C p(\tilde{\mathbf{v}}_i^{*k} | \boldsymbol{\theta}_c)}. \quad (33)$$

The sampling is repeated for as many cloud layers detected. All selected subsets of vectors, coordinate pairs, and weights, form the dataset that is used to approximate the wind velocity field,

$$\mathbf{X}^{*k} = \begin{bmatrix} x_1^{*k} & y_1^{*k} \\ \vdots & \vdots \\ x_{N^*}^{*k} & y_{N^*}^{*k} \end{bmatrix}, \quad \mathbf{V}^{*k} = \begin{bmatrix} \tilde{v}_1^{*k} & \tilde{u}_1^{*k} \\ \vdots & \vdots \\ \tilde{v}_{N^*}^{*k} & \tilde{u}_{N^*}^{*k} \end{bmatrix}, \quad \mathbf{Z}^{*k} = \begin{bmatrix} z_{1,1}^{*k} & z_{1,c}^{*k} \\ \vdots & \vdots \\ z_{N^*,1}^{*k} & z_{N^*,c}^{*k} \end{bmatrix}, \quad (34)$$

where  $N^k \gg N^*$ .

### 3 Flow Visualization

The atmosphere is a system where the dynamics are continuously changing [28]. This fact implies, that a wind velocity field exists, but we can only visualize it where clouds are present. The wind from the ground to the Tropopause can have multiple layers with different velocities in each one of the layers. Beside that, the wind flow can also be convective, however, for the sake of simplicity, we assume that the multi-layer flow which is observed in IR images is a multi-layer laminar flow. This is, the analysis neither consider z-component in the motion of a cloud, which is not observable, nor the possible inter-crossing of cloud layers.

#### 3.1 Wind Velocity Field Estimation

Three methods were implemented to estimate the extrapolation function and compare their performances. The first one uses a weighted  $\varepsilon$ -support vector regression machine ( $\varepsilon$ -WSVM) for each one of the velocity components. The second one is a multi-output  $\varepsilon$ -WSVM ( $\varepsilon$ -MO-SVM) that estimates both velocity components. The third is an innovation which uses a  $\varepsilon$ -MO-WSVM with flow constraints ( $\varepsilon$ -MO-WSVM-FC) to estimate both the velocity components, where the flow constraints are meant to force the extrapolated wind flow to have zero divergence or curl, so it can be assumed that, in the approximated wind flow, streamlines are equivalent to the cloud pathlines.

The regression problem can be formulated as the optimization of a function with the form,

$$f(\mathbf{x}_i) = \mathbf{w}^\top \varphi(\mathbf{x}_i) + b, \quad \forall i = 1, \dots, N^*, \quad \mathbf{w}, \mathbf{x}_i \in \mathbb{R}^D, \quad b \in \mathbb{R}. \quad (35)$$

where  $\mathbf{x}_i \triangleq \mathbf{x}_i^{*k}$  in our problem at hand, and where  $\varphi(\cdot)$  is a transformation into a higher dimensional (possibly infinite) Hilbert space  $\mathcal{H}$  endowed with a dot product  $\mathcal{K}(\mathbf{x}_i, \mathbf{x}_j) = \langle \varphi(\mathbf{x}_i), \varphi(\mathbf{x}_j) \rangle$ . A function  $\mathcal{K}(\mathbf{x}_i, \mathbf{x}_j)$  is a dot product if it is a bivariate positive semi-definite function that maps  $\mathbf{x}_i, \mathbf{x}_j$  into  $\mathbb{R}$ , commonly called a Mercer's kernel or simply a kernel function.

### 3.1.1 Support Vector Machine for Regression

Assuming  $\mathbf{v}_i = \{u_i, v_i\} \triangleq \mathbf{v}_i^{*k}$ , the regression problem in a  $\varepsilon$ -SVM is formulated with an  $\varepsilon$ -insensitive loss function, which penalizes the errors  $|\varepsilon| > 0$  [67, 52, 68] for each one of the components in  $\mathbf{v}_i$  and for each cloud layer  $c$  as

$$|u_i - f(\mathbf{x}_i)|_\varepsilon = \max[0, |u_i - f(\mathbf{x}_i)| - \varepsilon], \quad \forall i = 1, \dots, N, \quad u_i, \varepsilon \in \mathbb{R}, \quad (36)$$

and identically for  $v_i$ . The  $\varepsilon$ -insensitive loss function can be seen as a tube of radius  $\varepsilon$  adjusted around the regression hyper-plane via the Support Vectors (SV).

The samples are weighted by their probability of belonging to wind velocity field  $c$  [69, 70],

$$z_i \triangleq z_i^{*k}, \quad z_i \in \mathbb{R}^{\leq 1}. \quad (37)$$

$$c_i = z_i \cdot \frac{C}{N} \quad (38)$$

The L2-norm and  $\varepsilon$ -loss function is applied to the model weights,

$$\min_{\mathbf{w}, b, \xi, \xi^*} \quad \frac{1}{2} \|\mathbf{w}\|^2 + \frac{C}{N} \sum_{i=1}^N z_i (\xi_i + \xi_i^*) \quad (39)$$

$$\text{s.t.} \quad \begin{cases} u_i - \mathbf{w}^\top \varphi(\mathbf{x}_i) - b & \leq \varepsilon + \xi_i \\ \mathbf{w}^\top \varphi(\mathbf{x}_i) + b - u_i & \leq \varepsilon + \xi_i^* \\ \xi_i, \xi_i^* & \geq 0 \end{cases} \quad i = 1, \dots, N, \quad (40)$$

and identically for  $v_i$ . The slack variables  $\xi_i$  were introduced to relax the constrains of the optimization problem and to deal with unfeasible optimization problems [71, 54]. The primal objective function aims to find the trade off between the regularization term  $\varepsilon$ , the allowed errors or slack variables  $\xi_i$  and  $\xi_i^*$ , and the complexity of the model  $c_i$  per weighted sample.

The proposed kernel functions in this analysis are,

$$\mathcal{K}(\mathbf{x}_i, \mathbf{x}_j) = \mathbf{x}_i^\top \mathbf{x}_j, \quad (41)$$

$$\mathcal{K}(\mathbf{x}_i, \mathbf{x}_j) = \exp(-\gamma \cdot \|\mathbf{x}_i - \mathbf{x}_j\|^2), \quad (42)$$

$$\mathcal{K}(\mathbf{x}_i, \mathbf{x}_j) = (\gamma \cdot \mathbf{x}_i^\top \mathbf{x}_j + \beta)^d, \quad (43)$$

where  $\gamma, \beta \in \mathbb{R}$ , and  $d \in \mathbb{N}$  are the kernel hyperparameters that have to be cross-validated. These kernel functions are referred to as linear, radial basis function (RBF) or square exponential (SE), and polynomial of order  $d$  respectively [53].

In order to optimize the constrained problem in functional (39) and constraints (40) a Langrangian functional is constructed with the functional and the set of constrains through a dual set of new variables [54], which leads to a solvable Quadratic Programming problem (QP). The Lagrangian functional is

$$\mathcal{L}(\mathbf{w}, b, \alpha, \alpha^*, \beta, \xi, \xi^*, \varepsilon, \eta, \eta^*) = \quad (44)$$

$$= \frac{1}{2} \|\mathbf{w}\|^2 + c_i \sum_{i=1}^N (\xi_i + \xi_i^*) \dots \quad (45)$$

$$- \sum_{i=1}^N (\eta_i \xi_i + \eta_i^* \xi_i^*) - \sum_{i=1}^N \alpha_i (\varepsilon + \xi_i - u_i + \mathbf{w}^\top \varphi(\mathbf{x}_i) + b) \dots \quad (46)$$

$$- \sum_{i=1}^N \alpha_i^* (\varepsilon + \xi_i^* + u_i - \mathbf{w}^\top \varphi(\mathbf{x}_i) - b), \quad \forall i = 1, \dots, N, \quad \eta_i, \eta_i^* \in \mathbb{R}. \quad (47)$$

The derivatives of the primal variables  $\mathbf{w}, \varepsilon, \xi_i, \xi_i^*$  yield to the following set of equations, which is a case of Karush-Kuhn-Tucker (KKT) conditions,

$$\mathbf{w}^\top = \sum_{i=1}^N (\alpha_i^* - \alpha_i) \varphi(\mathbf{x}_i), \quad (48)$$

$$0 = \sum_{i=1}^N (\alpha_i - \alpha_i^*), \quad (49)$$

$$0 = c_i - \alpha_i - \eta_i, \quad (50)$$

$$0 = c_i - \alpha_i^* - \eta_i^*. \quad (51)$$



These conditions, together with the complimentary KKT conditions, which forces the product of dual parameters  $\alpha_i, \alpha_i^*$  with the constraints to be zero, leads, by substitution on the Lagrangian, to the following dual functional:

$$\min_{\alpha, \alpha^*} \quad \frac{1}{2} \cdot (\alpha - \alpha^*)^\top \mathbf{K} (\alpha - \alpha^*) + \sum_{i=1}^N (\alpha_i - \alpha_i^*) u_i + \varepsilon \cdot \mathbf{1}^\top (\alpha + \alpha^*) \quad (52)$$

$$\text{s.t.} \quad \begin{cases} \mathbf{1}^\top (\alpha - \alpha^*) = 0 \\ 0 \leq \alpha_i, \alpha_i^* \leq c_i \end{cases} \quad \forall i = 1, \dots, N. \quad (53)$$

where  $\mathbf{1}_{1 \times N} = [1, \dots, 1]^\top$ , and matrix  $\mathbf{K}$  is a Gram matrix of dot product such that  $\mathbf{K}_{i,j} = \mathcal{K}(\mathbf{x}_i, \mathbf{x}_j)$ . The minimization of the primal function is equivalent to find the saddle point on the Lagrangian formulation. The approximated function is,

$$f(\mathbf{x}) = \sum_{i=1}^N (\alpha_i - \alpha_i^*) \cdot \mathcal{K}(\mathbf{x}_i, \mathbf{x}_i) + b, \quad (54)$$

where  $b$  is obtained from the complimentary KKT conditions.

### 3.1.2 Multi-Output Weighted Support Vector Machine

When the wind velocity field function is approximated by  $\varepsilon$ -MO-SVM, the primal regression can be formulated as

$$\mathbf{v}_i = \mathbf{W}^\top \varphi(\mathbf{x}_i) + \mathbf{b}, \quad (55)$$

where each one of the column vectors of primal parameter matrix  $\mathbf{W}$  approximates one of the velocities in vector  $\mathbf{y}_i$ . Primal parameters are a function of the dual ones as well, but the dual parameters  $\alpha_i, \alpha_i^*$  are vectors in a 2-dimensional multi-output problem.

Since independent variables are represented in vectors  $\mathbf{v}_i$ , the training set is defined in a vector  $\tilde{\mathbf{v}}_{1 \times 2N}$ , and so are the dual parameters  $\tilde{\alpha}_{1 \times 2N}$  and  $\tilde{\alpha}_{1 \times 2N}^*$  for notation simplicity.

The gram matrix of dot products between input patterns  $\varphi(\mathbf{x}_i)$  can be interpreted as the covariance matrix between variables  $\mathbf{v}_i$ . Indeed

$$\begin{aligned} \mathbb{E}((\mathbf{v}_i - \mathbf{b}^\top)(\mathbf{v}_j - \mathbf{b})) &= \mathbb{E}(\mathbf{W}^\top \varphi(\mathbf{x}_i) \varphi(\mathbf{x}_j)^\top \mathbf{W}) \\ &= \begin{pmatrix} \varphi(\mathbf{x}_i)^\top \Sigma_{11} \varphi(\mathbf{x}_j) & \varphi(\mathbf{x}_i)^\top \Sigma_{12} \varphi(\mathbf{x}_j) \\ \varphi(\mathbf{x}_i)^\top \Sigma_{21} \varphi(\mathbf{x}_j) & \varphi(\mathbf{x}_i)^\top \Sigma_{22} \varphi(\mathbf{x}_j) \end{pmatrix}, \end{aligned} \quad (56)$$

where the  $2 \times 2$  covariance  $\mathbb{E}(\mathbf{W}\mathbf{W}^\top)$  is interpreted as a model for the dependencies between elements in  $\mathbf{v}_i$ , i.e.

$$\mathbb{E}(\mathbf{W}\mathbf{W}^\top) = \begin{pmatrix} \Sigma_{11} & \Sigma_{12} \\ \Sigma_{21} & \Sigma_{22} \end{pmatrix}. \quad (57)$$

If we consider that both vertical and horizontal velocities are independent, then  $\Sigma_{12} = \Sigma_{21} = \mathbf{0}$ . If we assume further that  $\Sigma_{11} = \Sigma_{22} = \mathbf{I}$  for simplicity, which, in turn leads to

$$\mathbb{E}((\mathbf{v}_i - \mathbf{b}^\top)(\mathbf{v}_j - \mathbf{b})) = \begin{pmatrix} \mathcal{K}(\mathbf{x}_i, \mathbf{x}_j) & 0 \\ 0 & \mathcal{K}(\mathbf{x}_i, \mathbf{x}_j) \end{pmatrix}. \quad (58)$$

The Gram matrix  $\tilde{\mathbf{K}}_{DN \times DN}$  in the  $\varepsilon$ -MO-SVM formulation for independent components is,

$$\tilde{\mathbf{K}} = \begin{pmatrix} \mathbf{K} & \mathbf{0} \\ \mathbf{0} & \mathbf{K} \end{pmatrix}. \quad (59)$$

The full kernel matrix in a  $\varepsilon$ -MO-WSVM is computationally expensive, and it is not implemented in this research.

The extension of weights in the  $\varepsilon$ -MO-WSVM requires to weight each sample in each output,

$$\tilde{z}_i = [z \dots z_N \ z_1 \dots z_N]^\top, \quad \sum_{i=1}^{D \cdot N} \tilde{z}_i = 2, \quad \tilde{z}_i \in \mathbb{R}^{\leq 1}. \quad (60)$$

The dual formulation of the QP problem for the  $\varepsilon$ -MO-WSVM is,

$$\min_{\tilde{\alpha}, \tilde{\alpha}^*} \quad \frac{1}{2} \cdot (\tilde{\alpha} - \tilde{\alpha}^*)^\top \tilde{\mathbf{K}} (\tilde{\alpha} - \tilde{\alpha}^*) + \tilde{\mathbf{y}}^\top (\tilde{\alpha} - \tilde{\alpha}^*) + \varepsilon \cdot \mathbf{1}^\top (\tilde{\alpha} + \tilde{\alpha}^*) \quad (61)$$

$$\text{s.t.} \quad \begin{cases} \mathbf{1}^\top (\tilde{\alpha} - \tilde{\alpha}^*) = 0 \\ \mathbf{0} \leq \tilde{\alpha}_i, \tilde{\alpha}_i^* \leq \tilde{c}_i \end{cases} \quad \forall i = 1, \dots, 2N, \quad (62)$$

where the extended weighted complexity is  $\tilde{c}_i = \tilde{z}_i / 2N$ .

### 3.1.3 Multi-Output Weighted Support Vector Machine with Flow Constrains

Based on the assumption that the analyzed air parcel is sufficiently small to consider that the flow is approximately incompressible and irrotational, a new set of flow constrains are added to the original set of constrains with the purpose of visualizing the wind velocity field to force that the divergence and the vorticity are both zero:

$$\text{s.t.} \begin{cases} \left( \tilde{\mathbf{v}}_c^{k\top} \Delta_{x,y} \dot{\mathbf{V}} \right) \cdot \left( \tilde{\mathbf{v}}_c^{k\top} \Delta_{x,y} \dot{\mathbf{V}} \right)^\top = 0 \\ \left( \tilde{\mathbf{v}}_c^{k\top} \Delta_{x,y} \dot{\mathbf{D}} \right) \cdot \left( \tilde{\mathbf{v}}_c^{k\top} \Delta_{x,y} \dot{\mathbf{D}} \right)^\top = 0, \end{cases} \quad (63)$$

where the matrices of this expression are defined as follows. In order to compute the vorticity and divergence, the differentiation of the velocity field along the x-axis, the and y-axis is implemented using operator

$$\Delta_{x,y} = \begin{bmatrix} \Delta_x & \mathbf{0} \\ \mathbf{0} & \Delta_y \end{bmatrix}_{2N \times 2N}, \quad (64)$$

where the differential operators  $\Delta_x$  and  $\Delta_y$  are defined as,

$$\Delta_x = \begin{bmatrix} -1 & 0 & \dots & 0 \\ 1 & -1 & \ddots & \vdots \\ 0 & 1 & \ddots & 0 \\ \vdots & \ddots & \ddots & -1 \\ 0 & \dots & 0 & 1 \end{bmatrix}_{N \times N}; \quad \Delta_y = \begin{bmatrix} -1 & \dots & 0 \\ \vdots & \ddots & \vdots \\ 0 & \dots & -1 \\ 1 & \dots & 0 \\ \vdots & \ddots & \vdots \\ 0 & \dots & 1 \end{bmatrix}_{N \times N}. \quad (65)$$

The operators of the velocity field's vorticity and divergence are respectively,

$$\dot{\mathbf{V}} = \begin{bmatrix} 1 & \dots & 0 \\ \vdots & \ddots & \vdots \\ 0 & \dots & 1 \\ 1 & \dots & 0 \\ \vdots & \ddots & \vdots \\ 0 & \dots & 1 \end{bmatrix}_{2N \times N}; \quad \dot{\mathbf{D}} = \begin{bmatrix} 1 & \dots & 0 \\ \vdots & \ddots & \vdots \\ 0 & \dots & 1 \\ -1 & \dots & 0 \\ \vdots & \ddots & \vdots \\ 0 & \dots & -1 \end{bmatrix}_{2N \times N}. \quad (66)$$

The extrapolated velocity field using the inferred parameters in frame  $k$  to the entire frame is

$$\hat{\mathbf{v}}_c^k = \left( \tilde{\boldsymbol{\alpha}}_c^k - \tilde{\boldsymbol{\alpha}}_c^{*k} \right) \cdot \mathcal{K}(\mathbf{X}^{*k}, \mathbf{X}) + \mathbf{b}_c^k, \quad (67)$$

where the velocity components are  $\hat{\mathbf{U}}_c^k \triangleq \hat{\mathbf{v}}_{x,c}^k$ , and  $\hat{\mathbf{V}}_c^k \triangleq \hat{\mathbf{v}}_{y,c}^k$ , where  $\hat{\mathbf{U}}_c^k, \hat{\mathbf{V}}_c^k \in \mathbb{R}^{M \times N}$ .

To compute the flow constrains, the velocity field have to be extrapolated to the whole frame using Eq. (67). The constrains in Eq. (63) are added to the constrains in the dual formulation of the  $\varepsilon$ -MO-SVM in Eq. (61).

## 4 Wind Velocity Field Dynamics Estimation

To estimate the wind velocity field dynamics, velocity vectors are approximated using the WLK method. The velocity vectors are weighted by the posterior probabilities of the cloud layers in the image, and transformed to the cloud layer plane. The velocity vectors are segmented and sampled to reduce the noise and the computation burden. The parameters of the  $\varepsilon$ -MO-WSVM-FC are cross-validated, and the model is trained to estimate the wind velocity field of the detected cloud layers. If an optimal set of parameters is available, it is possible to proceed with the training of  $\varepsilon$ -MO-WSVM-FM without performing the cross-validation. After training the  $\varepsilon$ -MO-WSVM-FC, the test is performed to extrapolate the wind velocity field to the whole image. The streamlines are computed using Eq. (68) to visualize the trajectory of a cloud. The potential lines are not shown in the Fig. 5a-6f, but they are computed with Eq. (69).

The physical process of cloud formation and evolution over time is part of atmosphere thermodynamics and may have divergence and vorticity [72]. Henceforth, the obtained results are a numerical approximation of the actual atmospheric air parcel flow. We consider that this is a feasible assumption because the air parcel in one of our frames is very small compared to the whole volume of air contained in the atmosphere.

When we assume that a flow does not have divergence and vorticity, the stream and the velocity potential functions are orthogonal, and we can apply the Cauchy-Riemann equations to calculate their rates of change [73]. For the stream function we determine  $d\phi = v_x dy - v_y dx$  using samples of functions. The trapezoidal rule of numerical analysis is applied to solve the definite integrals [74]. The values of a streamline are,

$$\Phi_c = \frac{\hat{H}_c}{2} \left[ \left\{ \sum_{m=1}^i \hat{\mathbf{u}}_{m,c} \odot \Delta \mathbf{y}_{m,c} \right\}_{i=1}^N - \left\{ \sum_{m=1}^j \hat{\mathbf{v}}_{m,c} \odot \Delta \mathbf{x}_{m,c} \right\}_{j=1}^N \right], \quad (68)$$

the sum of element-wise products between each velocity component, and its opposite increments, where  $\odot$  denotes the element-wise matrix multiplication.

The total change in the potential function is  $d\psi = v_x dx + v_y dy$ , so we can determine the potential in each pixel  $\mathbf{x} = \{x, y\}$  as,

$$\Psi_c = \frac{\hat{H}_c}{2} \left[ \left\{ \sum_{m=1}^j \hat{\mathbf{u}}_{m,c} \odot \Delta \mathbf{x}_{m,c} \right\}_{j=1}^N + \left\{ \sum_{m=1}^i \hat{\mathbf{v}}_{m,c} \odot \Delta \mathbf{y}_{m,c} \right\}_{i=1}^M \right]. \quad (69)$$

the sum of each element-wise product between the velocity components, and its differential increment.

## 5 Experiments

The proposed method for the inference of the wind velocity field utilizes data acquired by a system that captures circumsolar IR images at the same time that measures Global Horizontal Irradiance (GHI) using a pyranometer. The Data Acquisition system (DAQ) is equipped with a solar tracker that updates its pan and tilt every second, maintaining the Sun in a central position in the images along a day. The IR sensor is a Lepton<sup>1</sup> camera with radiometry, which has a wavelength from 8 to 14  $\mu m$  and provides a uniform thermal image. When the radiometry functionality is enabled, the pixels in a frame are turned into temperature measurements in centikelvin units. The resolution of an IR image is  $80 \times 60$  pixels, and the diagonal FOV is  $60^\circ$ .

The weather features that were used to compute the clouds height as well as to remove cyclostationary artifacts [50] on the IR images are: atmospheric pressure, air temperature, dew point and humidity. The weather station is set to measure every 10 minutes, so the data was interpolated to match the IR images sampling interval. The weather station is located at the University of New Mexico Hospital, and both its real-time and historical data are publicly accessible<sup>2</sup>.

The images in the top row of Fig. 1 show the temperature of the pixels obtained using the radiometric functionality of the IR camera in  $^\circ K$  (left pane), the height of the pixels in meters after applying the MALR transformation to the temperatures (center pane), and the temperature  $\bar{T}_{i,j}$  histogram in light blue color (right pane). Beta distributions in Eq. (1), are in red and blue, and the BeMM result in Eq. (3) is in black. The images in the bottom row show the temperature posterior probabilities  $\gamma_{i,j,1}$  of the upper layer (left), the temperature posterior probabilities  $\gamma_{i,j,2}$  of the lower layer (center), and the MAP classification of the pixels (right). In the image that shows the MAP classification of the pixels, the ones in dark blue color are the segmented pixels that do not belong to a cloud ( $b_{i,j} = 0$ ).

### 5.1 Training data construction

In order to construct a data set for validation purposes we randomly selected 21 consecutive images from six different days. Three of them were picked among those days that have one layer, and the other three among those that have two layers of clouds. The average cloud height, and magnitude and angle of the velocity vectors were manually calculated for each cloud layer in each sequence of images to use them as ground truth. To do that, the streamlines were manually segmented to measure which distance a cloud moved in each frame. The averaged height of the cloud layers were measured manually segmenting the clouds along the sequence of image. The height of each one of the cloud layer across the sequence of images was averaged.

### 5.2 Segmentation algorithm parameter validation

The parameters  $\delta$  in Eq. (10),  $\tau$  in Eq. (14),  $\ell$  in Eq. (15) of the velocity vectors selection algorithm were validated using the six sequences of images. The velocity estimator was  $\varepsilon$ -WSVM with a linear kernel. The parameters of

<sup>1</sup><https://www.flir.com/>

<sup>2</sup><https://www.wunderground.com/dashboard/pws/KNMALBUQ473>

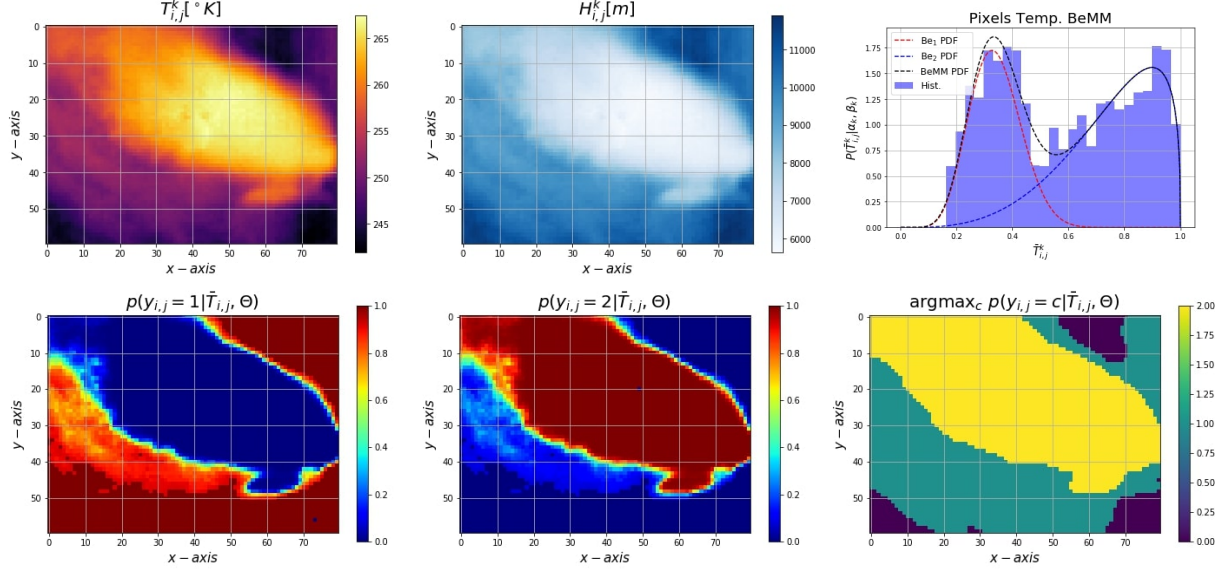


Figure 1: The images in the first row from left to right show the temperatures, their heights, and the BeMM distribution of the normalized temperatures. The images in the middle row shows the posterior probabilities of the upper layer, the posterior probabilities of the lower layer, and MAP classification of the pixels.

$\varepsilon$ -WSVM,  $\varepsilon$  and  $C$ , were cross-validated in the same process. The flow velocity constraints were not applied in the validation.

### 5.3 Velocity vector subsampling

The average of the approximated wind velocity field height, magnitude and angle was computed, and the Mean Absolute Percentage Error (MAPE) was calculated between the measured and the averaged approximation in each frame. The MAPE was averaged and differentiated across consecutive frames. The combination of parameters that had less averaged MAPE plus total difference of MAPE between consecutive frames was selected. This added cost was used to take into account the accuracy of the selected model parameters, but also the stability of this models. This stability is optimal if good results are consistently obtained for each one of the images in the same sequence.

The optimal amplitude  $\delta$  of the velocity vector in Eq. (10), was found to be  $\delta = 2.29$ . The optimal threshold  $\tau$  in the segmentation of the velocity vector in Eq. (14), was found to be  $\tau = 0.95$ . The optimal number of velocity vectors from  $\ell$  last frames to form the dataset in Eq. (15), was found to be  $\ell = 6$ . The optimal number of selected samples  $N^*$  by sampling algorithm in Eq. (34), was found that  $N^* = 200$  samples are sufficient to perform a robust extrapolation of the wind velocity field to the entire frame by the  $\varepsilon$ -MO-WSVM-FC.

The velocity vectors that were segmented in a frame with two layers of clouds are shown in Fig. 2. The velocity vectors from the last 6 frames after applying the segmentation are shown in the upper row of Fig. 3. In this figure, the colors represent the likelihoods, conditional to the upper cloud layer (left), and lower cloud layer (right). The sampled velocity vectors in a frame with two layers of clouds are shown in the bottom row. Fig. 4 shows the selected velocities in the bottom row of Fig. 3 in their corresponding coordinates. In this figure, the colors represent the posterior probabilities, conditional to the upper cloud layer (left), and lower cloud layer (right).

### 5.4 WSVM parameter validation

After optimal values of  $\delta$ ,  $\tau$  and  $\ell$  have been chosen, the parameters cross validation of the three proposed  $\varepsilon$ -WSVM to approximate the velocity field in a image is done separately using the same 4 days. A 75% of this data was chosen for training and validation. The rest of data was used for test. The test set is from  $k + \ell$  frames ahead of the training set from frame  $k$ . The number of frames ahead is equal to the lag of the velocity vectors in the data  $\ell = 6$ . The methodology implemented in the validation is the standard Grid Search (GS) and 3-fold cross-validation. The parameters cross-validated in the  $\varepsilon$ -WSVM are  $C$  and  $\varepsilon$ , and the kernel functions are: linear, RBF, polynomial of order two ( $P^2$ ), and polynomial of order three ( $P^3$ ). The optimal parameters for each  $\varepsilon$ -WSVM are displayed in Table 1.

### 5.5 Velocity field estimation in new data

The sets of optimal parameters obtained in cross validation are used to estimate the velocity field in four new different sequences of images. These new sequences are randomly picked from the days in our database that are ahead of those that were used in cross-validation. The experiments have two different set ups for each  $\varepsilon$ -WSVM. In the first one, the  $\varepsilon$ -WSVM parameters are cross-validated for each new frame. In the second one, the  $\varepsilon$ -WSVM parameters are fixed to the optimal values obtained in the previously explained parameter cross-validation. This is done to check for the validity of these previously obtain parameters, which would significantly reduce the velocity field estimation computational burden.

The most suitable  $\varepsilon$ -SVM and kernel function for our application is selected finding a trade-off between divergence and vorticity, Weighted Mean Absolute Error (WMAE), and the computing time. The values of these metrics are summarized in Table 1 for each  $\varepsilon$ -WSVC. The experiment of the  $\varepsilon$ -MO-WSVM without flow constrain using a  $\mathcal{P}^3$  kernel is shown in Fig. 5a, and that same experiment implemented with the  $\varepsilon$ -MO-WSVM-FC using a linear kernel is in Fig. 5b. In sequences of images in which two layers of clouds were detected, the experiments of the  $\varepsilon$ -MO-WSVM-FC using a linear kernel to approximate wind velocity field are shown in the Fig. 6a to 6f.

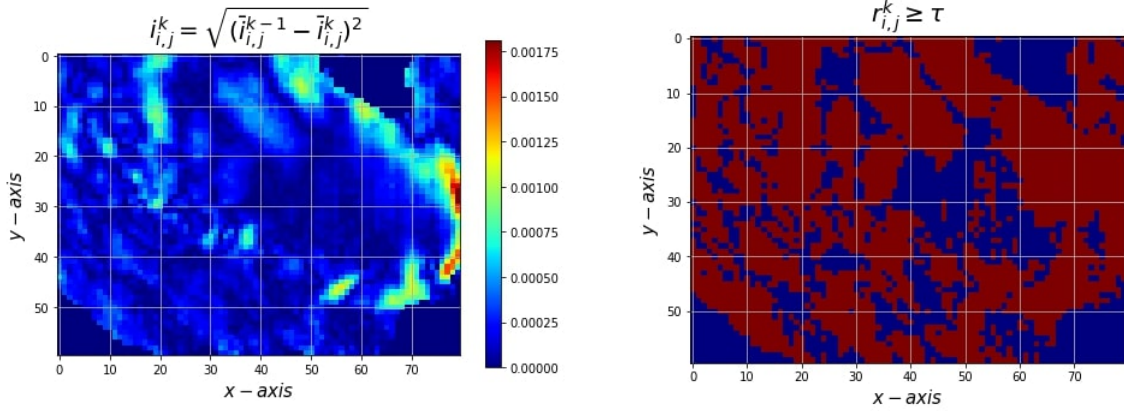


Figure 2: The graph on the left shows the variance between the normalized intensity  $i_{i,j}$  of the pixels in frame  $k$  and  $k - 1$ . The graph in the right shows the velocity vectors segmented  $r_{i,j}$ , applying  $\tau$ , defined as the total variance explained threshold.

The objective of the constrains is that the divergence and vorticity of approximated velocity field are zero in the clouds' plane. Nevertheless, the velocity field have divergence and vorticity when is projected to the camera plane. This is caused by the non-linear geometric transformation applied to the velocity field.

The experiments were carried out in the Wheeler high performances computer of UNM-CARC, which uses SGI AltixXE Xeon X5550 at 2.67GHz with 6 GB of RAM memory per core, has 8 cores per node, 304 nodes total, and runs at 25 theoretical peak FLOPS. It has installed Linux CentOS 7. The DAQ is localized on the roof area of UNM-ME building in Albuquerque, NM.

## 6 Discussion

This investigation adds a new insight in the computational methods to forecast the trajectory of clouds and foresee the occlusion of the Sun. The proposed method visualizes the wind velocity field using IR images of clouds. This algorithm differs from previous investigations in that it is based on fluid dynamics. The experiments show that the pathlines are equivalent to the streamlines in frames where is possible to extract enough information about the wind flow from the clouds.

From the summary of the experiments presented in Table 1, several aspects can be highlighted. The overall performance of the  $\varepsilon$ -SVM increases when the samples are weighted, since the weights represent the probability of the vector to belong to the corresponding layer. Vectors with a very low probability do not contribute to the solution. Furthermore, the computing time of the  $\varepsilon$ -WSVM is lower than the  $\varepsilon$ -MO-WSV as the Gram matrix dimensions are smaller. The flow divergence and vorticity is negligible when is approximated using the  $\varepsilon$ -MO-WSVM-FC, in contrast to its computing time, which is larger. The results are similar between the three models but the  $\varepsilon$ -MO-WSVM and  $\varepsilon$ -MO-WSVM-FC models tend to show better performance.

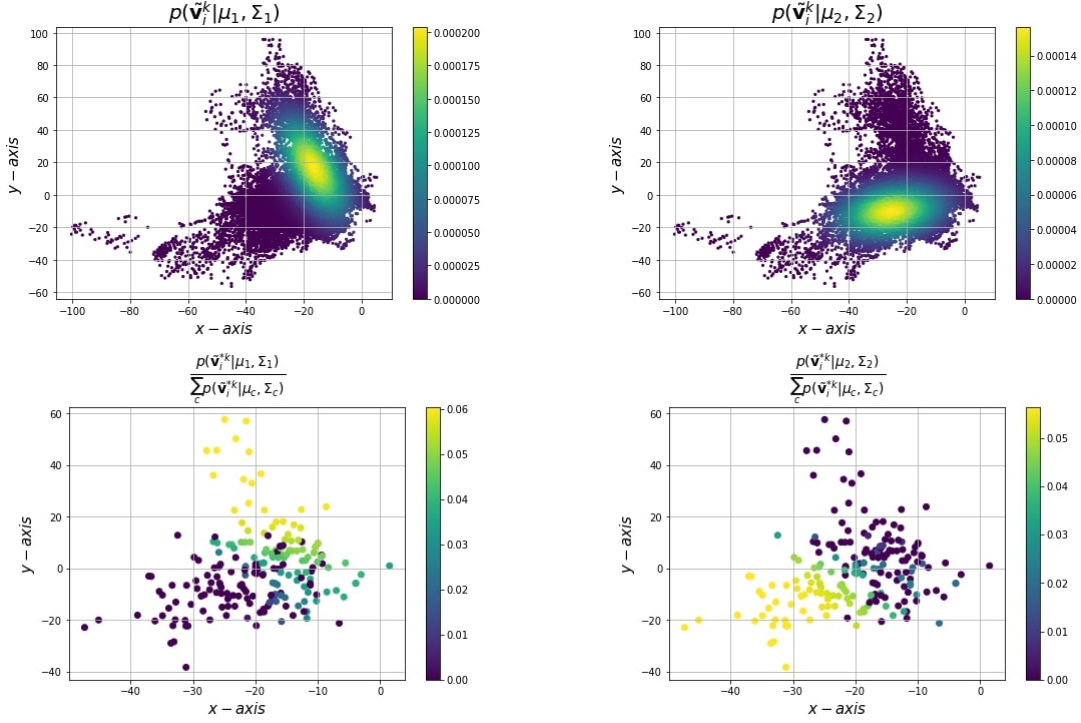


Figure 3: Top graphs show the inferred distributions of the velocity vectors. The dots are velocity vector samples, and their color is their probability in the cloud layer. Top left graph shows the distribution of the vectors in the upper cloud layer, and the right one the distribution of the vectors in the lower cloud layer. Bottom graphs show the downsampled set of vectors with their corresponding posterior probabilities.

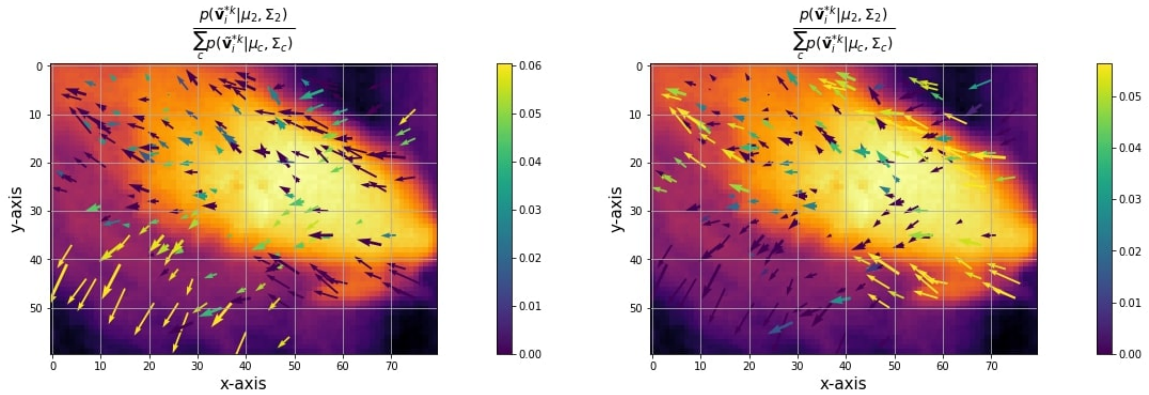


Figure 4: Vectors in the images show the velocities selected in Fig. 3 in their corresponding position. The left image vectors show a color intensity corresponding to their posterior probabilities conditional to the upper cloud layer and the right one to the lower layer.

The best result without cross-validation in WMAE is obtained by the  $\varepsilon$ -MO-WSVM-FC with RBF kernel (see Table 1). The flow approximated by this model has very low vorticity and divergence, which means that the pathlines and streamlines are approximately equivalent. When a trade-off is considered between vorticity, divergence, WMAE, and computing time, the most promising models are both the  $\varepsilon$ -MO-WSVM-FC with linear and RBF kernel. However, the computing time required for the linear kernel is lower, as the kernel does not have hyperparameters, but it is still high for a real-time application. Vorticity and divergence are removed in the approximated flow. On the other hand, the  $\varepsilon$ -WSVM with linear kernel, which has not flow constraints, is feasible in real-time application but the approximated flow is turbulent. When the pathlines begin to be the same as the streamlines, the flow constraints can be relaxed to reduce the vorticity and divergence within a feasible computing time.



$\varepsilon$ -SVM												
$\mathcal{K}(\mathbf{x}, \mathbf{x}^*)$	Parameters				Cross-Validated				Fixed			
	$C$	$\varepsilon$	$\gamma$	$\beta$	MAE	WMAE	$\nabla \cdot \vec{V}$	$\nabla \times \vec{V}$	MAE	WMAE	$\nabla \cdot \vec{V}$	$\nabla \times \vec{V}$
Linear	36.68	0.33			13.91	13.59	493.79	960.50	13.83	13.42	455.04	954.85
RBF	87.39	0.19	5.20		13.83	13.42	$6.38 \cdot 10^3$	$6.35 \cdot 10^3$	14.05	13.66	$1.03 \cdot 10^4$	$1.03 \cdot 10^4$
$\mathcal{P}^2$	33.11	0.31	4.78	24.45	16.83	16.48	$5.75 \cdot 10^4$	$5.69 \cdot 10^4$	26.15	25.98	$6.62 \cdot 10^4$	$7.21 \cdot 10^4$
$\mathcal{P}^3$	31.69	0.20	2.64	17.55	15.22	14.79	$1.36 \cdot 10^4$	$1.28 \cdot 10^4$	82.79	79.66	$3.97 \cdot 10^6$	$4.48 \cdot 10^6$
$\varepsilon$ -MO-WSVM												
Linear	31.06	0.31			13.53	13.35	375.11	895.40	13.34	13.06	465.13	957.10
RBF	38.71	0.36	17.81		13.81	13.32	$1.03 \cdot 10^3$	$1.01 \cdot 10^3$	13.40	13.09	631.24	631.87
$\mathcal{P}^2$	34.73	0.28	4.65	10.66	13.92	13.53	$2.18 \cdot 10^3$	$2.72 \cdot 10^3$	22.57	22.11	$9.11 \cdot 10^4$	$7.20 \cdot 10^4$
$\mathcal{P}^3$	38.47	0.22	4.19	2.33	26.90	23.50	$4.53 \cdot 10^5$	$5.74 \cdot 10^5$	35.73	35.88	$5.42 \cdot 10^5$	$8.11 \cdot 10^5$
$\varepsilon$ -MO-WSVM-FC												
Linear	38.50	0.19			13.47	13.31	0	0	13.57	13.32	0	0.01
RBF	38.52	0.35	13.92		14.09	13.72	24.48	24.25	13.65	13.31	131.74	132.01
$\mathcal{P}^2$	39.72	0.24	3.78	44.8	14.37	13.96	61.06	98.00	15.10	14.75	477.77	367.05
$\mathcal{P}^3$	12.88	0.22	5.61	8.34	61.65	63.62	$3.30 \cdot 10^7$	$3.53 \cdot 10^7$	51.43	50.40	$2.22 \cdot 10^6$	$2.19 \cdot 10^6$

Table 1: Summary of the experiments with an independent  $\varepsilon$ -WSVM for each one of the velocity components, and the  $\varepsilon$ -MO-WSVM and  $\varepsilon$ -MO-WSVM-FC for both velocity components. The table shows the cross-validated optimal parameters, plus the results obtained when the parameters were cross-validated and when they were fixed to the optimal during the test sequences.

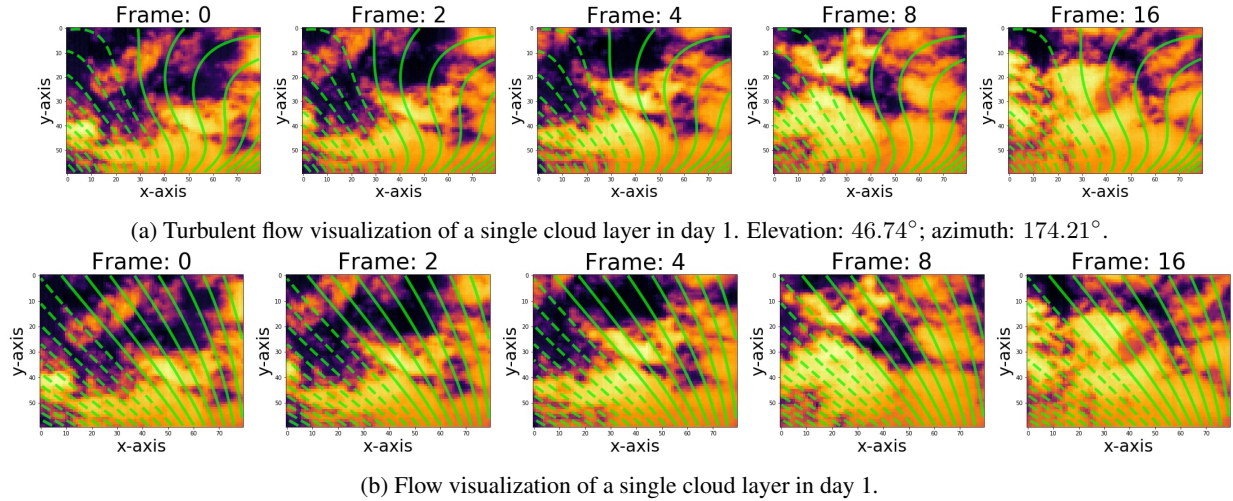


Figure 5: The IR images are organized chronologically from the left to the right. The time between frames is 15 s. The distance in the sequences across time is: 0 s, 30 s, 1 min 2 min 4 min. The sequence shows a day when a single cloud layer was detected. In Fig. 5a, the streamlines and potential lines were approximated using the  $\varepsilon$ -MO-WSVM with a  $\mathcal{P}^3$  kernel. In Fig. 5b, the flow was approximated using the  $\varepsilon$ -MO-WSVM-FC with a linear kernel. The top sequence visualizes a non-realistic approximation of the flow. A compression is induced to the gas in the bottom left of the frame, and an expansion is induced in the top right of the frame.

In the implementation of the algorithm, the process of cross-validating the parameters of the  $\varepsilon$ -MO-WSVM-FC is computationally expensive, plus the kernels might have hyperparameters which also require cross-validation. However, the optimal set of parameters is of the same order of magnitude during sort sequences. We propose to implement an exhaustive cross-validation in parallel with the running of the algorithm. This way, there will be pre-computed set of

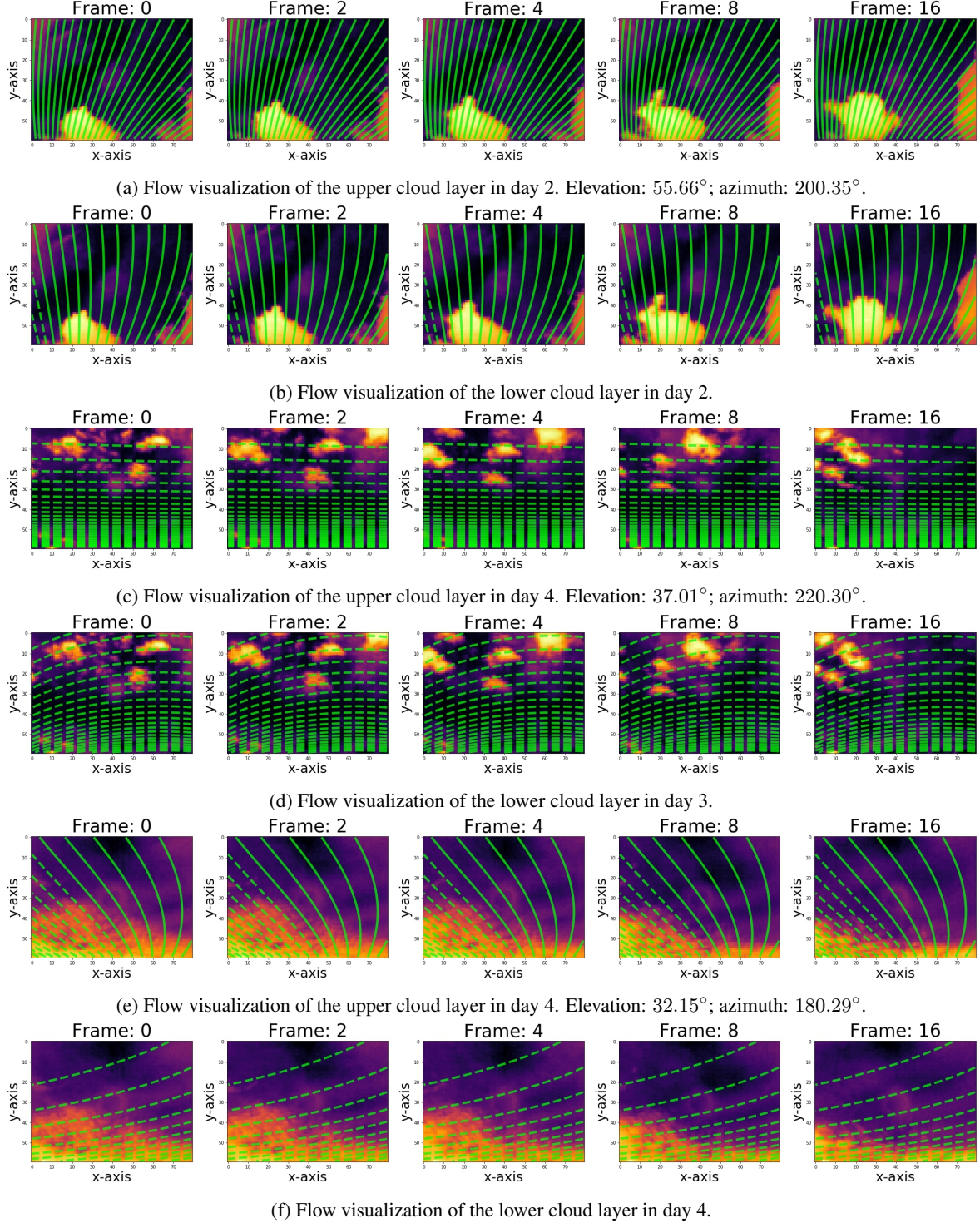


Figure 6: The sequence of IR images are organized chronologically from the left to the right similar to in Fig. 5a and 5b. The sequence displayed are from days when two different cloud layers were detected. The upper layer of clouds is displayed in the top row of the sequence, whilst in the bottom row is displayed the lower layer. The streamlines and potential lines were approximated using the  $\varepsilon$ -MO-WSVM-FC with a linear kernel.

parameters for the  $\varepsilon$ -MO-WSVM-FC and the kernel function, which can be used in the consecutive frames until the online cross-validation is finished.



## 7 Conclusions

This article introduces a method to visualize wind velocity fields with physical features extracted from clouds. This method utilizes IR images of clouds. The images are recorded using a ground-based IR camera mounted on a solar tracker that maintains the Sun in the center of the images. The velocity vectors are transformed from the Euclidean frame of reference to the IR camera non-linear frame of reference. The wind velocity field estimation is based on unsupervised learning methods that infer independently the distribution of the velocity vectors and the height of the clouds. The segmentation and a subsampling of velocity vectors provides a computationally tractable solution. The wind velocity field is extrapolated to the entire frame using only information extracted from a cloud. This is achieved with the use of a  $\varepsilon$ -MO-WSVM which includes flow constraints in the QP problem formulation.

The methods to compute the motion vectors produce a noisy approximation of the velocity vectors in the frame. It is possible to improve the quality of the velocity vectors adding weights to the WLS solution in the WLK, and later segmenting the velocity vectors. Once the noise is reduced, a subsample of vectors is sufficient to approximate the velocity field in the entire frame. This makes feasible a real-time implementation of the algorithm for wind flow visualization. This is important because the visualization of the wind velocity field predicts the pathlines of the clouds. The extrapolation of the wind velocity field to the entire frame is useful to anticipate where a cloud will be, or where it may appear in the frame. The additional constraints in the SVM yields better results, approximating the wind velocity field in the IR images.

Further research this area may focus on the implementation of a pixel's selection and feature extraction algorithm in the application of GSI forecast. This algorithm may be based on the visualization of a wind flow with multiple layers of clouds. In the existing literature there are multiple optimization algorithms that might speed up the convergence of the  $\varepsilon$ -MO-WSVM-FC. The prediction of the wind velocity field distribution across space and time using Bayesian regression methods is suitable for the selection of the most likely intercepting pixels.

## 8 Acknowledgments

This work has been supported by NSF EPSCoR grant number OIA-1757207 and the King Felipe VI endowed Chair. Authors would like to thank the UNM Center for Advanced Research Computing, supported in part by the National Science Foundation, for providing the high performance computing and large-scale storage resources used in this work.

## References

- [1] CEC. Clean energy and pollution reduction act - sb 350, 2016.
- [2] ANRE. Feed-in tariff for renewable electricity and solar pv auction, 2017.
- [3] EC. Renewable energy directive 2018/2001/eu, 2018.
- [4] IEA. Snapshot of global photovoltaic markets, 2015.
- [5] Jan Beyea. The smart electricity grid and scientific research. *Science*, 328(5981):979–980, 2010.
- [6] C. Wan, J. Zhao, Y. Song, Z. Xu, J. Lin, and Z. Hu. Photovoltaic and solar power forecasting for smart grid energy management. *CSEE Journal of Power and Energy Systems*, Dec 2015.
- [7] Xiaoyang Chen, Yang Du, Enggee Lim, Huiqing Wen, Ke Yan, and James Kirtley. Power ramp-rates of utility-scale pv systems under passing clouds: Module-level emulation with cloud shadow modeling. *Applied Energy*, 268:114980, 2020.
- [8] Arda Halu, Antonio Scala, Abdulaziz Khiyami, and Marta C González. Data-driven modeling of solar-powered urban microgrids. *Science advances*, 2(1), 2016.
- [9] Maimouna Diagne, Mathieu David, Philippe Lauret, John Boland, and Nicolas Schmutz. Review of solar irradiance forecasting methods and a proposition for small-scale insular grids. *Renewable and Sustainable Energy Reviews*, 27(Supplement C):65 – 76, 2013.
- [10] Jui-Sheng Chou and Ngoc-Son Truong. Cloud forecasting system for monitoring and alerting of energy use by home appliances. *Applied Energy*, 249:166 – 177, 2019.
- [11] Kari Lappalainen and Seppo Valkealahti. Output power variation of different pv array configurations during irradiance transitions caused by moving clouds. *Applied Energy*, 190:902 – 910, 2017.
- [12] D. Mateos, M. Antón, A. Valenzuela, A. Cazorla, F.J. Olmo, and L. Alados-Arboledas. Efficiency of clouds on shortwave radiation using experimental data. *Applied Energy*, 113:1216 – 1219, 2014.

- [13] Francesco Crespi, Andrea Toscani, Paolo Zani, David Sánchez, and Giampaolo Manzolini. Effect of passing clouds on the dynamic performance of a csp tower receiver with molten salt heat storage. *Applied Energy*, 229:224 – 235, 2018.
- [14] Dazhi Yang, Jan Kleissl, Christian A. Gueymard, Hugo T.C. Pedro, and Carlos F.M. Coimbra. History and trends in solar irradiance and pv power forecasting: A preliminary assessment and review using text mining. *Solar Energy*, 168:60 – 101, 2018. Advances in Solar Resource Assessment and Forecasting.
- [15] Claudia Furlan, Amauri Pereira de Oliveira, Jacyra Soares, Georgia Codato, and João Francisco Escobedo. The role of clouds in improving the regression model for hourly values of diffuse solar radiation. *Applied Energy*, 92:240 – 254, 2012.
- [16] H. Escrig, F.J. Batlles, J. Alonso, F.M. Baena, J.L. Bosch, I.B. Salbidegoitia, and J.I. Burgaleta. Cloud detection, classification and motion estimation using geostationary satellite imagery for cloud cover forecast. *Energy*, 55(Supplement C):853 – 859, 2013.
- [17] H. S. Jang, K. Y. Bae, H. S. Park, and D. K. Sung. Solar power prediction based on satellite images and support vector machine. *IEEE Transactions on Sustainable Energy*, 2016.
- [18] Richard Perez, Sergey Kivalov, James Schlemmer, Karl Hemker Jr., David Renné, and Thomas E. Hoff. Validation of short and medium term operational solar radiation forecasts in the us. *Solar Energy*, 2010.
- [19] Clara Arbizu-Barrena, José A. Ruiz-Arias, Francisco J. Rodríguez-Benítez, David Pozo-Vázquez, and Joaquín Tovar-Pescador. Short-term solar radiation forecasting by advecting and diffusing msg cloud index. *Solar Energy*, 155(Supplement C):1092 – 1103, 2017.
- [20] A. Hammer, D. Heinemann, E. Lorenz, and B. Lückehe. Short-term forecasting of solar radiation: a statistical approach using satellite data. *Solar Energy*, 1999.
- [21] R. Ineichen, P. Perez. Derivation of cloud index from geostationary satellites and application to the production of solar irradiance and daylight illuminance data. *Theoretical and Applied Climatology*, 1999.
- [22] C. Schillings, H. Mannstein, and R. Meyer. Operational method for deriving high resolution direct normal irradiance from satellite data. *Solar Energy*, 2004.
- [23] Hou Jiang, Ning Lu, Guanghui Huang, Ling Yao, Jun Qin, and Hengzi Liu. Spatial scale effects on retrieval accuracy of surface solar radiation using satellite data. *Applied Energy*, 270:115178, 2020.
- [24] Abhnil A. Prasad, Robert A. Taylor, and Merlinde Kay. Assessment of direct normal irradiance and cloud connections using satellite data over australia. *Applied Energy*, 143:301 – 311, 2015.
- [25] A. Mammoli, A. Ellis, A. Menicucci, S. Willard, T. Caudell, and J. Simmins. Low-cost solar micro-forecasts for pv smoothing. In *2013 1st IEEE Conference on Technologies for Sustainability (SusTech)*, pages 238–243, 2013.
- [26] Hugo T.C. Pedro and Carlos F.M. Coimbra. Assessment of forecasting techniques for solar power production with no exogenous inputs. *Solar Energy*, 86(7):2017 – 2028, 2012.
- [27] Cyril Voyant, Gilles Notton, Soteris Kalogirou, Marie-Laure Nivet, Christophe Paoli, Fabrice Motte, and Alexis Fouilloy. Machine learning methods for solar radiation forecasting: A review. *Renewable Energy*, 105(Supplement C):569 – 582, 2017.
- [28] Eugenia Kalnay. *Atmospheric Modeling, Data Assimilation and Predictability*. Cambridge University Press, 2003.
- [29] O. García-Hinde, G. Terrén-Serrano, M.Á. Hombrados-Herrera, V. Gómez-Verdejo, S. Jiménez-Fernández, C. Casanova-Mateo, J. Sanz-Justo, M. Martínez-Ramón, and S. Salcedo-Sanz. Evaluation of dimensionality reduction methods applied to numerical weather models for solar radiation forecasting. *Engineering Applications of Artificial Intelligence*, 69:157 – 167, 2018.
- [30] CN Long, DW Slater, and Tim P Tooman. *Total sky imager model 880 status and testing results*. Pacific Northwest National Laboratory Richland, Wash, USA, 2001.
- [31] M.I. Gohari, B. Urquhart, H. Yang, B. Kurtz, D. Nguyen, C.W. Chow, M. Ghonima, and J. Kleissl. Comparison of solar power output forecasting performance of the total sky imager and the university of california, san diego sky imager. *Energy Procedia*, 49, 2014.
- [32] Chi Wai Chow, Bryan Urquhart, Matthew Lave, Anthony Dominguez, Jan Kleissl, Janet Shields, and Byron Washom. Intra-hour forecasting with a total sky imager at the uc san diego solar energy testbed. *Solar Energy*, 2011.
- [33] Ricardo Marquez and Carlos F.M. Coimbra. Intra-hour dni forecasting based on cloud tracking image analysis. *Solar Energy*, 2013.

- [34] Pascal Kuhn, Stefan Wilbert, Christoph Prah, David Schüler, Thomas Haase, Tobias Hirsch, Michael Wittmann, Lourdes Ramirez, Luis Zarzalejo, Angela Meyer, et al. Shadow camera system for the generation of solar irradiance maps. *Solar Energy*, 157:157–170, 2017.
- [35] R. Chauvin, J. Nou, S. Thil, A. Traoré, and S. Grieu. Cloud detection methodology based on a sky-imaging system. *Energy Procedia*, 2015.
- [36] Hsu-Yung Cheng. Cloud tracking using clusters of feature points for accurate solar irradiance nowcasting. *Renewable Energy*, 104:281–289, 2017.
- [37] H.M. Deneke, A.J. Feijt, and R.A. Roebeling. Estimating surface solar irradiance from meteosat seviri-derived cloud properties. *Remote Sensing of Environment*, 112(6):3131 – 3141, 2008.
- [38] Andrea Mammoli, Guillermo Terren-Serrano, Anthony Menicucci, Thomas P Caudell, and Manel Martínez-Ramón. An experimental method to merge far-field images from multiple longwave infrared sensors for short-term solar forecasting. *Solar Energy*, 187:254–260, 2019.
- [39] Tore Wizelius. *Developing wind power projects: theory and practice*. Earthscan, 2007.
- [40] Todd S Glickman and Walter Zenk. *Glossary of meteorology*. AMS (American Meteorological Society), 2000.
- [41] William J Randel, Fei Wu, and Dian J Gaffen. Interannual variability of the tropical tropopause derived from radiosonde data and ncep reanalyses. *Journal of Geophysical Research: Atmospheres*, 105(D12):15509–15523, 2000.
- [42] Joseph A. Shaw, Paul W. Nugent, Nathan J. Pust, Brentha Thurairajah, and Kohei Mizutani. Radiometric cloud imaging with an uncooled microbolometer thermal infrared camera. *Opt. Express*, 13(15):5807–5817, Jul 2005.
- [43] Joseph A. Shaw and Paul W. Nugent. Physics principles in radiometric infrared imaging of clouds in the atmosphere. *European Journal of Physics*, 34(6):S111–S121, oct 2013.
- [44] Nathan J. Pust Paul W. Nugent, Joseph A. Shaw. Correcting for focal-plane-array temperature dependence in microbolometer infrared cameras lacking thermal stabilization. *Optical Engineering*, 52(6):1 – 8 – 8, 2013.
- [45] B. Thurairajah and J. A. Shaw. Cloud statistics measured with the infrared cloud imager (ici). *IEEE Transactions on Geoscience and Remote Sensing*, 43(9):2000–2007, Sep. 2005.
- [46] Paul W. Nugent, Joseph A. Shaw, and Sabino Piazzolla. Infrared cloud imaging in support of earth-space optical communication. *Opt. Express*, 17(10):7862–7872, May 2009.
- [47] Chia-Lin Fu and Hsu-Yung Cheng. Predicting solar irradiance with all-sky image features via regression. *Solar Energy*, 97:537–550, 2013.
- [48] Weicong Kong, Youwei Jia, Zhao Yang Dong, Ke Meng, and Songjian Chai. Hybrid approaches based on deep whole-sky-image learning to photovoltaic generation forecasting. *Applied Energy*, 280:115875, 2020.
- [49] C. Deng, Z. Li, W. Wang, S. Wang, L. Tang, and A. C. Bovik. Cloud detection in satellite images based on natural scene statistics and gabor features. *IEEE Geoscience and Remote Sensing Letters*, 16(4):608–612, April 2019.
- [50] Guillermo Terrén-Serrano and Manel Martínez-Ramón. Data acquisition and image processing for solar irradiance forecast, 2020.
- [51] Ibrahim Reda and Afshin Andreas. Solar position algorithm for solar radiation applications. *Solar Energy*, 76(5):577 – 589, 2004.
- [52] Bernhard Schölkopf, Alexander Smola, Er Smola, and Klaus-Robert Müller. Nonlinear component analysis as a kernel eigenvalue problem. *Neural Computation*, 10:1299–1319, 1998.
- [53] John Shawe-Taylor and Nello Cristianini. *Kernel Methods for Pattern Analysis*. Cambridge University Press, New York, NY, USA, 2004.
- [54] Alex J. Smola and Bernhard Schölkopf. A tutorial on support vector regression. *Statistics and Computing*, 14(3):199–222, August 2004.
- [55] Vladimir N. Vapnik. *Statistical Learning Theory*. Wiley-Interscience, 1998.
- [56] Iyyanki V. Muralikrishna and Valli Manickam. Chapter fourteen - air pollution control technologies. In *Environmental Management*, pages 337 – 397. Butterworth-Heinemann, 2017.
- [57] Kevin P. Murphy. *Machine Learning: A Probabilistic Perspective*. The MIT Press, 2012.
- [58] Christopher M. Bishop. *Pattern Recognition and Machine Learning*. Springer, 2006.
- [59] Jorge Nocedal and Stephen J. Wright. *Numerical Optimization*. Springer, New York, NY, USA, second edition, 2006.

- [60] B. D. Lucas and T. Kanade. An iterative image registration technique with an application to stereo vision, 1981.
- [61] Berthold KP Horn and Brian G Schunck. Determining optical flow. *Artificial intelligence*, 17(1-3):185–203, 1981.
- [62] Gunnar Farneback. Two-frame motion estimation based on polynomial expansion. *Image analysis*, pages 363–370, 2003.
- [63] L. Adrian, R.J. Adrian, and J. Westerweel. *Particle Image Velocimetry*. Cambridge Aerospace Series. Cambridge University Press, 2011.
- [64] Simon Baker, Ralph Gross, Takahiro Ishikawa, and Iain Matthews. Lucas-kanade 20 years on: A unifying framework: Part 2. *International Journal of Computer Vision*, 56:221–255, 2003.
- [65] Johan Ludwig William Valdemar Jensen et al. Sur les fonctions convexes et les inégalités entre les valeurs moyennes. *Acta mathematica*, 30:175–193, 1906.
- [66] Julian Besag. On the statistical analysis of dirty pictures. *Journal of the Royal Statistical Society B*, 48(3):48–259, 1986.
- [67] Harris Drucker, Christopher J. C. Burges, Linda Kaufman, Alex J. Smola, and Vladimir Vapnik. Support vector regression machines. In M. C. Mozer, M. I. Jordan, and T. Petsche, editors, *Advances in Neural Information Processing Systems 9*, pages 155–161. MIT Press, 1997.
- [68] Bernhard Schölkopf, Alex J. Smola, Robert C. Williamson, and Peter L. Bartlett. New support vector algorithms. *Neural Comput.*, 12(5):1207–1245, May 2000.
- [69] Ehab E. Elattar, John Goulermas, and Q. H. Wu. Electric load forecasting based on locally weighted support vector regression. *Trans. Sys. Man Cyber Part C*, 40(4):438–447, 7 2010.
- [70] Xixuan Han and Line Clemmensen. On weighted support vector regression. *Quality and Reliability Engineering*, 10 2014.
- [71] Corinna Cortes and Vladimir Vapnik. Support-vector networks. In *Machine Learning*, pages 273–297, 1995.
- [72] D. Lamb and J. Verlinde. *Physics and Chemistry of Clouds*. Cambridge University Press, 2011.
- [73] R.A. Granger. *Fluid Mechanics*. Dover Books on Physics. Dover Publications, 1995.
- [74] Sever S Dragomir, Pietro Cerone, and Anthony Sofo. Some remarks on the trapezoid rule in numerical integration. *RGMIA research report collection*, 2(5), 1999.